Numerical Analysis of Micro-Lens Array to the Mid-IR Range †

Ricardo Gonzalez-Romero [1,*] , **Guillermo Garcia-Torales** [1] and **Marija Strojnik** [2]

1   University Center for Exact Sciences and Engineering, University of Guadalajara, Av. Revolución No. 1500, Guadalajara 44430, Mexico; garcia.torales@academicos.udg.mx
2   Optical Research Center, A. P. 1-948, Leon 37000, Mexico; mstrojnik@gmail.com
*   Correspondence: jaimer.gonzalezr@academicos.udg.mx
†   Presented at the 16th International Workshop on Advanced Infrared Technology & Applications, 26–28 October 2021; Available online: https://aita2021.sciforum.net/.

Abstract: New interferometric IR techniques have recently been developed to allow Sun-Jupiter-like detections in deep space. These techniques demand a high angular resolution, a high sensitivity towards signal detection buried in noise, and a well-defined bandwidth of spectral resolution. Micro-lens arrangements have helped increase the use of these parameters for IR detectors. In this paper we present a finite element method (FEM)-based simulation of a typical micro-lens array, to be used in mid-IR cameras, where the aperture geometry and radius of curvature are varied for design optimization. Moreover, we show the spot and optical aberrations produced by two types of geometrical arrangements. This procedure could be helpful in improving the IR detector signal in the exoplanets exploration, in systems placed outside of the earth's atmosphere.

Keywords: micro-lens array; FEM; finite element method; IR detectors; mid-IR

1. Introduction

Exoplanetary searches have increased in importance in recent years, due to advancements in the interferometric detection techniques outside of the Earth's atmosphere [1–3]. However, these techniques require a high angular resolution and a high sensitivity towards signals buried in noise, as well as a well-defined spectral bandwidth and resolution [4]. Micro-lens arrays can improve some parameters of IR detectors for the IR interferometry, and reduce problems originating inside the optical system, such as wavefront correction and issues with the field of view (FOV), to name a few [5–7].

Micro-lens arrays are arrangements of small-size lenses, called lenslets, distributed side by side to cover the surface of a CCD sensor, where portability is mandatory. A lenslet generally has a circular aperture, due to its easy construction. However, this circular aperture includes a non-active area in the array, due to the distance between two lenslets, that results in an efficiency deterioration. Furthermore, part of the radiation is incident out-of-focus on another pixel, producing crosstalk. Some of the design parameters, such as the radius of curvature, the geometry of the aperture, and the lens material, may be analyzed using a finite element method (FEM). This procedure was employed recently to evaluate the aberrations and the spot in the focal plane.

In this paper, we present a numerical analysis, based on FEM, for a micro-lens array with two different apertures—circular and square—and two radii of curvature. The analysis was performed on an MIR wavelength, used in exoplanetary detection, λ_i = 9.492 µm [8].

2. Materials and Methods

Each lenslet was a convexo-planar lens, due to their easy fabrication. We performed two numerical studies for two different types of lenslet apertures (circular and square) and two frontal radii of curvature.

Figure 1 shows a single lenslet of the array. The focal plane located at the focal distance for the test wavelength $f(\lambda_i)$ represents the sensor surface. The lens maker's

formula indicates the focal length as a function of the radii of curvature, R_{ai} and R_b, the refractive index for lens material and surrounding medium, $n(\lambda_i)$, and $n(\lambda_s)$, respectively, and the micro-lens thickness, P.

$$f(\lambda_i) = \left\{ [\beta]\frac{1}{R_{ai}} - \frac{1}{R_b} + \frac{P\beta}{n(\lambda_i)R_{ai}R_b} \right\}^{-1}, \tag{1}$$
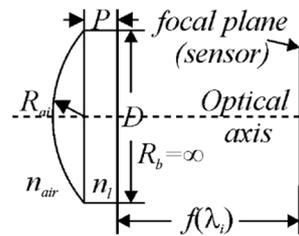
Figure 1. Each lenslet is convexo-planar, with a flat base width of $P = 3.7$ μm, placed at the focal length $f(\lambda_1) = 1.23$ μm for study one, and $f(\lambda_2) = 2.46$ μm for study two, from the surface sensor. The radius of curvature is $R_{a1} = 3.7$ μm, with a circular aperture for the first study. For the second study, the radius of curvature is $R_{a2} = 7.4$ μm. The circular aperture of diameter D has a value of $2R_{a1}$. The side of the square aperture is equal to R_{a2}.

Here, $\beta = n(\lambda_i) - n(\lambda_s)$. Equation (1) is valid for any wavelength, refractive indices, and radii of curvature of the lens. In our case, the source wavelength was $\lambda_i = 9.492$ μm, corresponding to the mean wavelength for exoplanetary exploration. The surrounding material was vacuum ($n(\lambda_s) = 1$), and the lens material was Ge ($n(\lambda_i) = 4.0044$). R_{ai} was the radius of curvature for the front surface, with values of $R_{a1} = 3.7$ μm for study one, and $R_{a2} = 7.4$ μm for study two. The radius of the curvature for the back surface was $R_b = \infty$ for both studies, considering that this surface was flat. The lenslet thickness was $P = 3.7$ μm, which corresponded to the minimum commercial size. The aperture $D = 2R_{a1}$ had a circular shape for study one, and a square shape with sides equal to R_{a2} for study two.

Figure 2 shows the micro-lens arrangements for the two cases of studies. The total size of the array corresponded to one-tenth of the commercial dimensions of the CCD sensor, with 160 × 120 pixels. Each pixel had dimensions 7.4 × 7.4 μm, or 118.4 × 88.8 μm for 16 × 12 pixels. We planned for 10 × 10 sub-arrays of micro-lenses, joined side by side, to complete the minimum size for the sensor surface. The aperture for study one was circular, as shown in Figure 2a. The lenslet in study two was square in form, as shown in Figure 2b. The geometric aperture changes between the studies had the purpose of decreasing the non-active area between the micro-lenses where the light was incident, but was not imaged on the sensor surface.
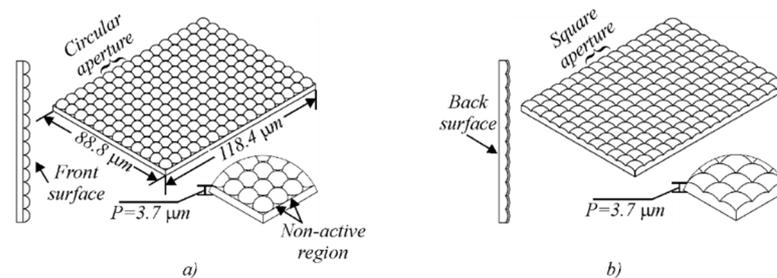
Figure 2. (**a**) Matrix of 12 × 16 elements with the radius of curvature $R_{a1} = 3.7$ μm and circular aperture of $D = 2R_{a1}$. (**b**) Matrix of 12 × 16 elements with the radius of curvature $Ra_2 = 7.4$ μm and square aperture with a side size of $D = R_{a2}$.

The FEM model used in this investigation is described in [9]. The Zernike polynomials in their polar form with σ as the radial distance, are shown in [10]. The non-polarized light

source modeled had λ_i = 9.492 µm, placed at 15 µm from the lenslet surface, a spot radius of about 44.4 µm, an intensity of 3.18 [mW/cm^2], and an hexapolar normal distribution.

3. Results

A finite element simulation was performed for each case study, employing the same wavelength, initial, and boundary conditions. In study one, the lenses had a circular aperture and a curvature radius of 3.7 µm. In study two, the lenses had a square aperture to avoid non-active areas, and a curvature radius of 7.4 µm.

3.1. RMS Spot Size

Figure 3 shows the spots at the focal plane for case studies one and two. A black circle indicates the root mean square value of the radius of the spot. The colors represent the ray as a function of the traveled distance from the source. This representation implies the energy distribution, and which rays contributed to the wavefront and crosstalk error. The RMS spot radius for case one (the square aperture) was only 298 nm larger than for case two (circular aperture). This difference indicated that there was no apparent change in the image on the sensor surface using a square aperture. However, when using the square aperture, more energy was concentrated on the sensor surface by filling in the non-active regions, improving the image quality. Moreover, the light focusing efficiency was almost the same for studies one and two, with values of 33.44% and 33.41%, respectively.
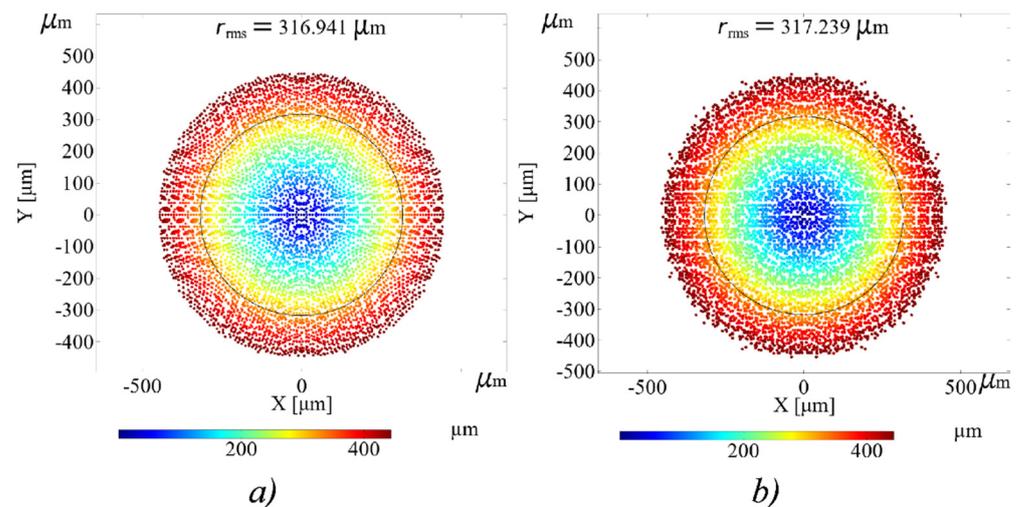

Figure 3. Spot images at the focal plane: (**a**) circular and (**b**) square aperture. The black circle indicates the RMS spot radius. The colors represent the lateral ray displacement from the point on the aperture to the position on the focal plane, and its contribution to wavefront and crosstalk error.

3.2. Optical Aberrations

Figure 4 shows the aberrations for case studies one and two. The piston and defocus aberrations have been eliminated because their contribution may have been eliminated during alignment. The values shown in the legend are the wavefront error in µm. As expected, the wavefront errors for study two were smaller than for study one; 400 times lower for the maximum error (dark blue) and 804 times smaller for the minimum error (dark red).

The vertical aberration tilt, vertical coma, and spherical aberration were the most significant in comparison to the other aberrations in both studies. However, the vertical tilt aberration can be corrected by alignment, and does not affect the image quality. The vertical coma aberration indicated a difference in the radii of curvature between the periphery and the central zones. As expected, the vertical coma was not significant in case two. Finally, the spherical aberration indicated the difference between the focal lengths for the periphery and the center. As shown in Figure 4a, the error was concentrated at the center and the

border. Nevertheless, as shown in Figure 4b, the relative error was distributed over the entire micro-lens array. However, these were smaller in magnitude for the second case than for the first case in study one.
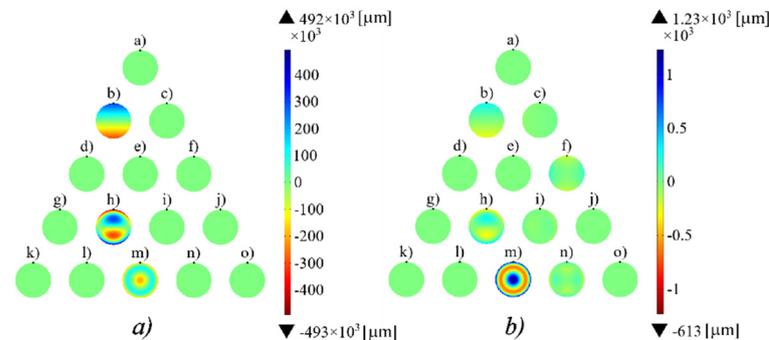
Figure 4. Aberration diagrams for (**a**) circular and (**b**) square apertures, with the piston and defocus aberrations eliminated. The values shown in the legend are the wavefront error in μm. The wavefront errors for study two are 400 times lower for the maximum error (in dark blue) and 804 times smaller for the minimum error (in dark red) than for the study one.

4. Conclusions

The FEM analysis applied for the determination of the aberration and the focal image at the sensor surface produced by a micro-lens array is a valuable tool in lenslet design. The micro-lens array with the square lenslet aperture reduced the crosstalk and results in a decreasing wavefront error, by eliminating the non-active surface areas between lenslets. FEM analysis allows for the optimization of optical design to improve IR detection in interferometric systems.

References

1. Gonzalez-Romero, R.; Strojnik, M.; Garcia-Torales, G.; Gomez-Rosas, G. Frequency Dependence of a Piezo-Resistive Method for Pressure Measurements of Laser-Induced Shock Waves in Solids. *Photonics* **2021**, *8*, 120. [CrossRef]
2. Galan, M.; Strojnik, M.; Garcia-Torales, G.; Kirk, M.S. Telescope Array for Extrasolar Planet Detection from the Far Side of the Moon. *Appl. Opt.* **2016**, *55*, D173–D180. [CrossRef] [PubMed]
3. Strojnik, M.; Scholl, M.K. Extrasolar Planet Observatory on the Far Side of the Moon. *J. Appl. Remote Sens.* **2014**, *8*, 1–9. [CrossRef]
4. Montes-Flores, M.; Garcia-Torales, G.; Strojnik, M. A Lab Proof-of-Concept of an Extrasolar Planet Detection Using a Rotationally Shearing Interferometer. *Proc. SPIE* **2021**, *11830*, 118300O.
5. Leger, J.R.; Scott, M.L.; Bundman, P.; Griswold, M.P. Astigmatic Wavefront Correction of a Gain-Guided Laser Diode Array Using Anamorphic Diffractive Microlenses. In *Computer-Generated Holography II*; Lee, S.H., Ed.; SPIE: Los Angeles, CA, USA, 1988; Volume 0884, pp. 82–89.
6. Ratcliff, J.; Supikov, A.; Alfaro, S.; Azuma, R. ThinVR: Heterogeneous Microlens Arrays for Compact, 180 Degree FOV VR near-Eye Displays. *IEEE Trans. Vis. Comput. Graph.* **2020**, *26*, 1981–1990. [CrossRef] [PubMed]

7. Scholl, M.S. *Optical Analysis of Segmented Aperture Averager*; SPIE: Los Alamos, CA, USA, 1981; Volume 0288.
8. Strojnik, M. *Optimal Wavelength Interval for Extra-Solar Planet Detection*; SPIE: San Diego, CA, USA, 2021; Volume 11830.
9. Gonzalez-Romero, R.; García-Torales, G.; Strojnik, M. *Spatial Distribution Analysis of Two-Dimensional Microlens Arrays by Finite Element Method*; SPIE: San Diego, CA, USA, 2021; Volume 11830.
10. Lakshminarayanan, V.; Fleck, A. Zernike Polynomials: A Guide. *J. Mod. Opt.* **2011**, *58*, 545–561. [CrossRef]